New test of time-reversal invariance in ^{19}Ne beta decay*

F. P. Calaprice,† E. D. Commins, and D. C. Girvin

Physics Department and Lawrence Berkeley Laboratory, University of California, Berkeley, California 94720

A new experimental upper limit on the "time-reversal" coefficient D is reported for the allowed beta decay ^{19}Ne → ^{19}F + e^+ + ν_e. The result, expressed in terms of the relative phase angle between axial-vector (A) and vector (V) couplings, is $\phi_{A,V}(^{19}\text{Ne}) = 180.2 \pm 0.4°$, consistent with T invariance. A nuclear-spin-polarized atomic beam of ^{19}Ne in which either of the magnetic substates $m_I = \pm \frac{1}{2}$ can be selected, is allowed to terminate its flight in a cell, where the ^{19}Ne atoms remain for approximately four seconds without substantial spin depolarization. Delayed coincidences between positrons and ^{19}F-recoil ions from decays in the cell are observed and correlated with nuclear spin to determine D. The ^{19}Ne nuclear polarization is monitored continuously by observation of the beta-decay asymmetry.

I. INTRODUCTION

We report here an improved experimental test of time-reversal (T) invariance in the allowed beta decay

$$^{19}\text{Ne} \to {}^{19}\text{F}^- + e^+ + \nu_e \quad (t_{1/2} = 17.36 \text{ sec}),$$

in which a search is made for a "triple" correlation of the form $\vec{J} \cdot \vec{p}_e \times \vec{p}_\nu$ between the initial nuclear spin and the momenta of the final leptons.[1] In an earlier experiment[2,3] the search was carried out by observations of delayed coincidences between ^{19}F⁻ recoil ions and positrons, from the decay-in-flight of a polarized atomic beam of ^{19}Ne. Similar experiments have also been performed with polarized beams of neutrons.[4]

In the present work, the polarized ^{19}Ne beam is allowed to terminate its flight in a cell, where the atoms remain for approximately four seconds without suffering appreciable nuclear-spin-depolarization. Observations of decays in the cell yield determinations of the positron asymmetry and neutrino asymmetry as well as the triple correlation. In the latter two cases the long cell sitting time allows greatly enhanced counting rates as compared to those obtained with decays in flight. Thus we have been able to achieve a four-fold improvement in the precision of the triple correlation measurement.

The experiment may be understood from consideration of the differential transition probability $d\lambda$ for decay of polarized ^{19}Ne, (nuclear spin $J = \frac{1}{2}$). Using the approximation where all final-state electromagnetic corrections and momentum-transfer-dependent terms in the beta-decay matrix element are neglected, and summing over final lepton spins, we have

$$d\lambda = \frac{G^2 \cos^2\theta}{(2\pi)^5} F(Z,E) (E_0 - E)^2 pE \, dE d\Omega_e d\Omega_\nu$$

$$\times \xi \left\{ 1 + a_0 \vec{v} \cdot \hat{q} + \frac{\langle \vec{J} \rangle}{J} \cdot [A\vec{v} + B\hat{q} + D\vec{v} \times \hat{q}] \right\}. \quad (1)$$

Here we employ units where $\hbar = c = 1$. Also, G is the Fermi coupling constant, θ is the Cabibbo angle, $F(Z,E)$ is the positron-spectrum Coulomb correction, and E_0 is the maximum e^+ energy, while $\vec{p}$, $\vec{v}$, and E are the positron momentum, velocity, and energy, respectively. Also, $\hat{q}$ is a
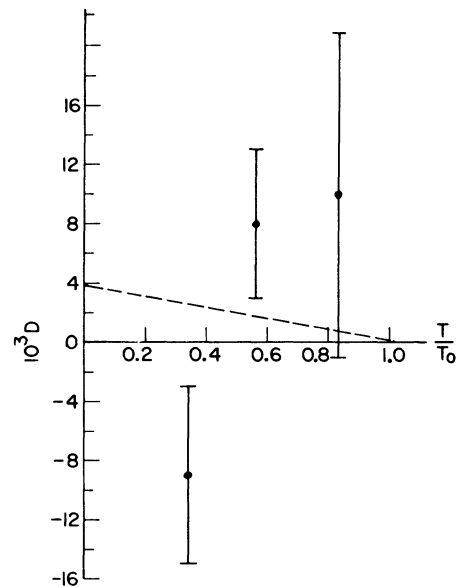
FIG. 1. Theoretical D is plotted vs. electron kinetic energy T in units of maximum kinetic energy $T_0 = 2.21$ MeV (dashed line) assuming Ima*$d = 10$, Ima*$c = 0$, and the CVC hypothesis. The points with vertical error bars correspond to measurements of D for the energy intervals δE_1, δE_2, δE_3 as defined in text.

unit vector in the direction of neutrino momentum, $d\Omega_e$ and $d\Omega_\nu$ are differential solid angles for positron and neutrino, respectively, and $\langle \vec{J}\rangle/J$ defines the initial nuclear polarization. The quantities ξ, A, B, and D are given by the formulas:

$$\xi = |a|^2 + |c|^2 , \tag{2}$$

$$A = \frac{+\frac{2}{3}|\rho|^2 + (2/\sqrt{3})|\rho|\cos\phi}{1 + |\rho|^2} , \tag{3}$$

$$B = \frac{-\frac{2}{3}|\rho|^2 + (2/\sqrt{3})|\rho|\cos\phi}{1 + |\rho|^2} , \tag{4}$$

$$D = \frac{-(2/\sqrt{3})|\rho|\sin\phi}{1 + |\rho|^2} , \tag{5}$$

where $a = C_V M_F$, $c = C_A M_{GT}$, and $\rho \equiv |\rho|e^{i\phi} = a/c$. For $|\rho| = 1.60 \pm 0.01$ as determined from $ft(^{19}\mathrm{Ne})$, we find $D = -(0.519 \pm 0.001)\sin\phi$.

From previous measurements it is already known that $\phi \simeq \pi$. Time-reversal invariance requires ρ to be real, hence $D = 0$, when final-state corrections are neglected.[5] Equations (1)–(5) have been generalized by Holstein,[6] who has considered corrections due to momentum-dependent terms and final-state electromagnetic effects. The corrections to ξ, A, and B are negligible for our purposes. In the case of D, our experimental result is

$$D_{\mathrm{expt}}(^{19}\mathrm{Ne}) = 0.002 \pm 0.004 \tag{6}$$

so that the corrections are not negligible *a priori*. In fact, Holstein finds a contribution of about 2×10^{-4} to D arising from final-state effects, in agreement with earlier estimates.[3] As for momentum-dependent terms, Holstein has shown that
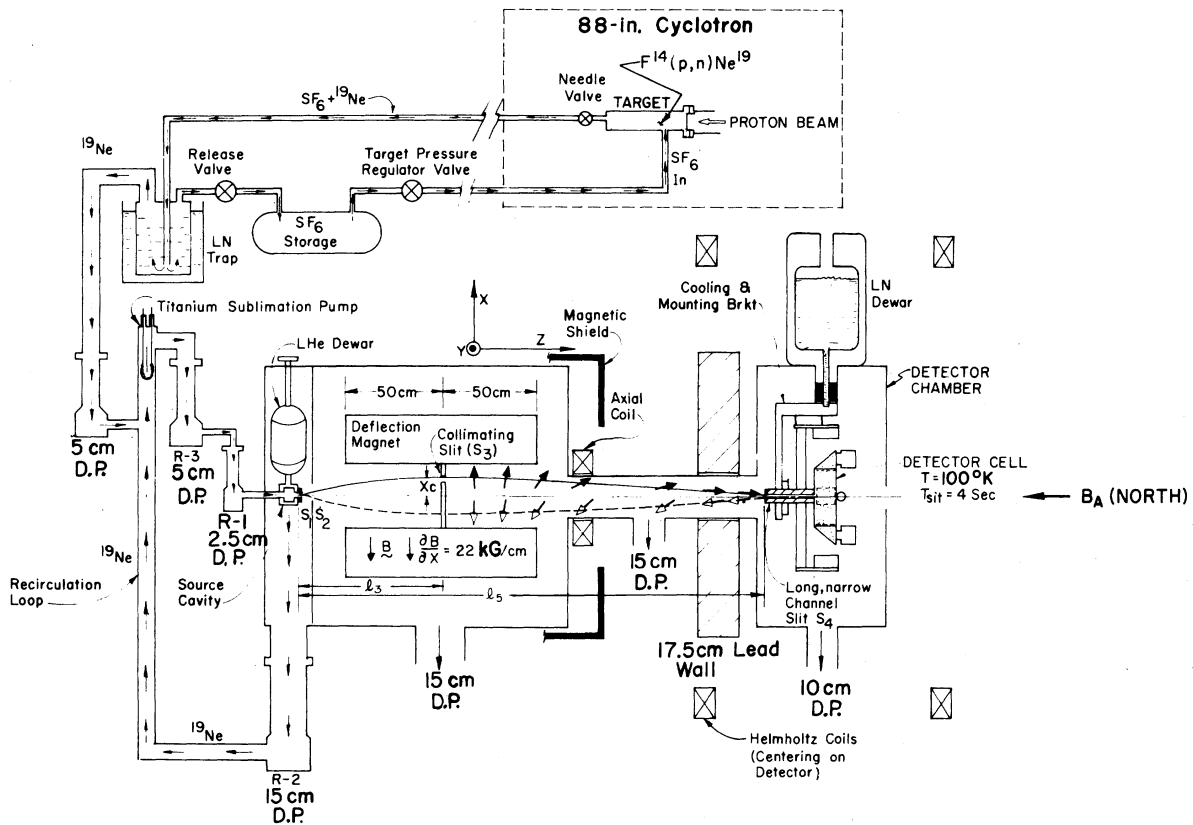
FIG. 2. Schematic diagram of apparatus (not to scale). $^{19}\mathrm{Ne}$ is produced by the reaction $^{19}\mathrm{F}(p,n)^{19}\mathrm{Ne}$ with 15-MeV protons from the LBL 88-in. cyclotron in a target containing SF_6 gas at ~ 1.5 atm pressure. SF_6 is continuously circulated through the target and carries $^{19}\mathrm{Ne}$ to an LN_2 trap, where SF_6 is removed. The target and experimental areas are separated by massive concrete shielding. $^{19}\mathrm{Ne}$ continues from trap to atomic beam source at 30 °K. The beam is formed by effusion from slit S_1 and collimated by slit S_3, the position of which determines m_I; dark (light) arrows represent the orientation of the $^{19}\mathrm{Ne}$ *nuclear moment* (antiparallel to spin) as atoms pass through S_3 for $x_c > 0$ (< 0). The moments follow adiabatically the changing orientation of the magnetic fields. In the "D" experiment the spins are rotated from transverse to longitudinal orientation with the axial coil. In the "B" experiment the spins remain transverse. The beam deflections are grossly exaggerated for clarity. The actual collimator deflection on either side of the center line is 0.076 cm, while the beam length is about 1.5 m.

$$\bar{D}(^{19}\text{Ne}) \simeq (\tfrac{1}{3})^{1/2} \frac{1}{|a|^2 + |c|^2} \text{Im} a^* \left(2c + \frac{E_0}{M} d\right), \quad (7)$$

where $M = \tfrac{1}{2}[M(^{19}\text{Ne}) + M(^{19}\text{F})]$, d is the so-called induced tensor contribution to the hadronic weak current matrix element, the validity of the conserved vector current (CVC) hypothesis is assumed, and the bar over D indicates an average over the e^+ energy spectrum (see Fig. 1). Equation (7) is identical to Eq. (5) except for the additional term in d.

Note that for a mirror transition such as ^{19}Ne $\rightarrow$ ^{19}F, the terms a and c are first class, while d is second class with respect to G-parity transformations.[7] As pointed out by Kim and Primakoff and others,[8] the charge-symmetry condition then implies that $\text{Im} a^* c = 0$ even if T invariance is violated. If this is the case, then a nonzero D could only arise from a nonzero value of $\text{Im} a^* d$. Since $E_0/M \simeq 10^{-4}$, one would require $\text{Im} a^* d \simeq 10$ if it were to contribute an observable amount to D at the present level of experimental precision.

Our work has been motivated by the discovery of CP violation in K_L decay, which is consistent with, but by no means implies, a T-odd weak amplitude of relative size $\simeq 10^{-3}$ ("milliweak" interaction). A review of the various theoretical proposals offered to explain CP violation has been summarized by Wolfenstein.[9] A recent summary of experimental data is given by Fitch.[10]

II. EXPERIMENTAL METHOD

A. Source of polarized neon-19

Neon-19 is produced at the LBL 88-in. cyclotron, transported to the experimental apparatus, and formed into a nuclear-spin-polarized atomic beam in the $^1S_0$ atomic ground state by a method described in detail in Ref. 3 (see Fig. 2). Beta decays are observed in a detector cell into which the atomic beam enters through a long narrow channel (length 7.6 cm, width 0.076 cm, height 0.95 cm). Neon-19 atoms strike the inner surfaces of the detector, fill the detector volume uniformly, and eventually decay or are pumped out of the channel into the vacuum (5×10^{-7} Torr) surrounding the cell. The sitting time in the cell is determined by the cell volume and channel conductance. It was chosen at 4 sec ($\simeq 10^{+5}$ wall collisions per atom in the cell) to give a reasonable probability of decay within the cell without excessive loss of polarization by wall collisions, etc. The cell was designed so that observations of D could be carried out with polarization parallel or antiparallel to the beam axis, while B observations required polarization perpendicular

to the beam axis. The beam polarization as initially formed (by a "Stern-Gerlach" magnet) is transverse. This is maintained by a homogeneous magnetic field in the x direction in Fig. 2, generated by large square coils centered on the cell (not shown in Fig. 2), for B measurements. In the case of D, the polarization is rotated from transverse to longitudinal with the aid of an axial steering coil (see Fig. 2) and the magnetic field in the cell, generated by a pair of Helmholtz coils 1.52 m in diameter and centered on the cell, is in the z direction and homogeneous to better than one part in 10^4 over the cell volume. For all measurements the sign of spin polarization can be reversed by motion of a collimating slit in the Stern-Gerlach magnet. (See Fig. 3.) This has
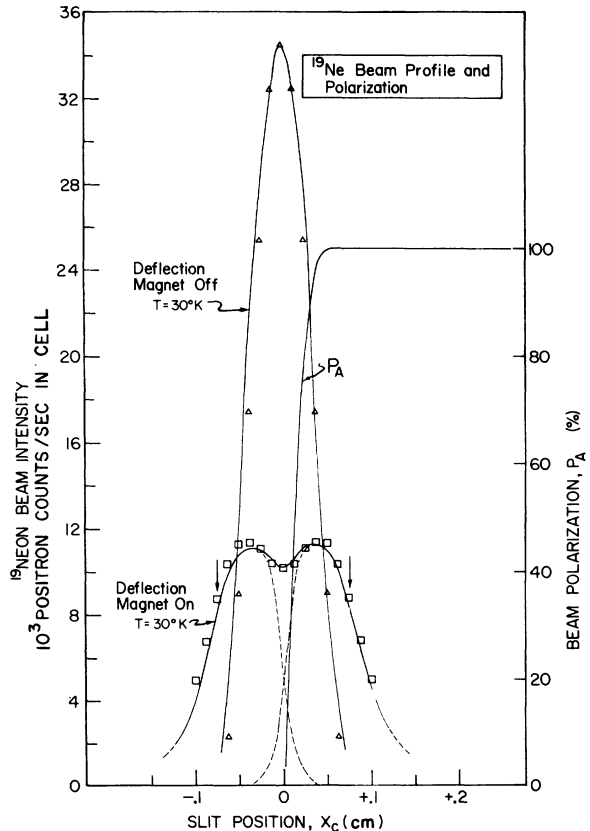
FIG. 3. Beam intensity and polarization at entrance to detector cell. The solid curves are calculated using $\mu(^{19}\text{Ne}) = -1.88\mu_N$, a source temperature of 30 °K, and a deflection magnetic field gradient of 22 kG/cm. Experimental points are shown as triangles and squares. x_c is the distance from the magnet center line to the center of the collimating slit, which is 0.076 cm wide. For $x_c > 0.076$ cm the polarization of the beam is 100%. Arrows indicate locations of the collimator-slit center line used to select opposite spin states in the actual experiment.
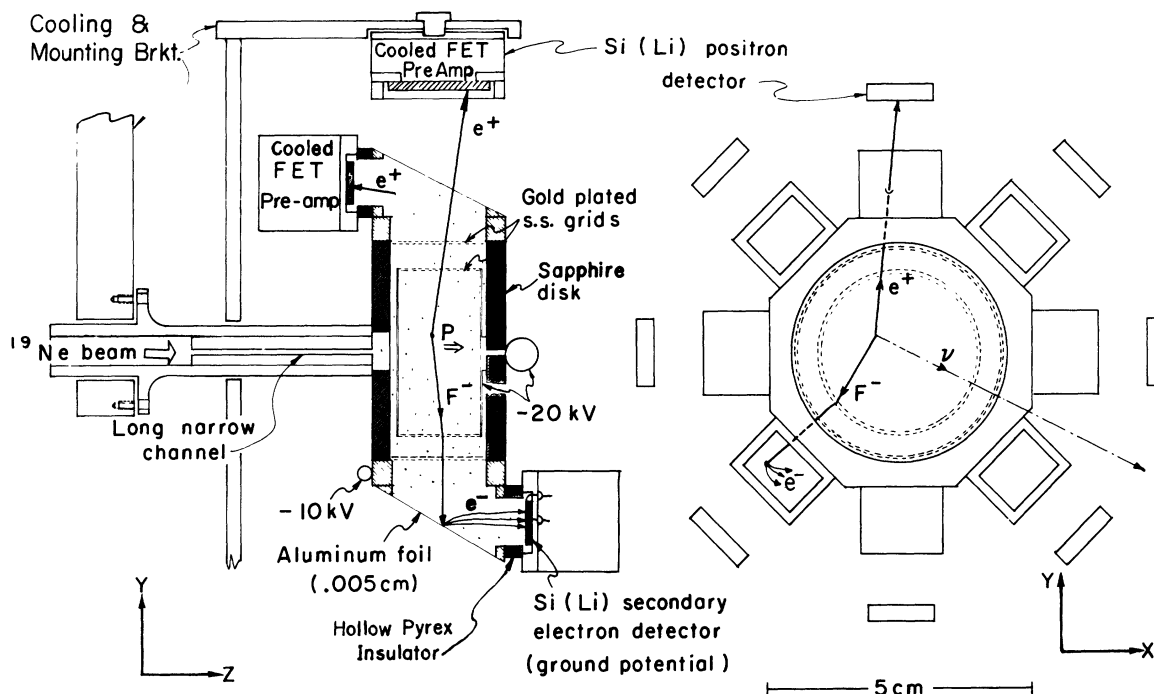
FIG. 4. Side and end view of octagonal cell detector assembly. Converter boxes are shown in end view as rectangles mounted on octagon, with openings to Si detectors alternately facing along the $\pm z$ axis. Inner and outer grids are shown as double dashed lines. The detector functions in the D experiment as follows. After entering the cell through a long narrow copper channel, ^{19}Ne atoms (shown as dots) are uniformly distributed throughout the cell volume. Particle trajectories from a typical decay within inner grid are shown in both views. The positron passes through the foil, while the ion drifts radially toward the edge of the inner grid. The radial acceleration of the ion is followed by secondary electron (e^-) production upon ion impact with the foil. The nuclear spin of ^{19}Ne, denoted as P, is maintained by a magnetic field $\vec{B}_A = \pm\hat{z}\,|B_A|$. Positrons originating from decays within converter boxes and passing through the Si (secondary-electron) detectors provide a 350-keV signal. Such a decay is shown at top left. Measurement of these 350-keV singles counts provides continuous monitoring of the polarization.

negligible effect on the beam trajectory at the channel entrance, and requires no reversal of magnetic fields.

B. Detector cell

Figures 4 and 5 show the detector cell in more detail. The hollow Al frame (A in Fig. 5) on which the cell is constructed forms an octagon 2.54 cm in length with a centered 4.76-cm i.d. hole along the symmetry axis. Eight equally spaced rectangular holes are milled in the octagon as shown. On the outer octagon faces are mounted 8 Al converter boxes (B) and ion detectors (D). These assemblies face alternately in opposite directions. Lapping and silicone vacuum grease provide vacuum seals between adjoining faces. The top of each converter box, formed from a 0.005-cm Duralumin foil, provides a window through which positrons may leave the cell. Ions striking the foil stop and eject secondary electrons which are accelerated by an electrostatic field (to be described below) allowing detection of the ion. The

foil is glued to the box with Shell 828 resin epoxy.

The ends of the octagon are sealed by sapphire disks (E) 4.76 cm in diameter and 0.22 cm thick. Positron detectors (G) are mounted externally to the cell on a machined bracket which ensures over-all alignment.

The inner grid (H) is 1.90 cm long and 3.80 cm in diameter. It consists of two concentric cylinders of a fine mesh gold-plated stainless steel screen (23.6 lines per cm, 90% transparency, manufactured by Buckbee Mears Company) mounted on the inner and outer surfaces of a metal cylinder of thickness 0.16 cm with rectangular holes. The inner grid is mounted along the bulb axis by a pin through the center of the sapphire disk and is thus electrically insulated from the rest of the cell.

The volume within the inner grid (26% of the total cell volume) is electric-field-free and is maintained at −20 kV. It defines the region from which coincidence events are accepted.

The outer grid (I), formed in a similar manner

A- Al Octagon (-10 kV)
B- Converter Box (-10 kV)
C- Pyrex Insulator
D- Ion Detector & FET Box (Ground Potential)
E- Sapphire Disks
F- Beam Entrance Channel (Ground Potential)
G- Positron Detector & FET Box (Ground Potential)
H- Double Layer Inner Grid (-20 kV)
I - Double Layer Outer Grid (-10 kV)
J - 20kV High Voltage Connector
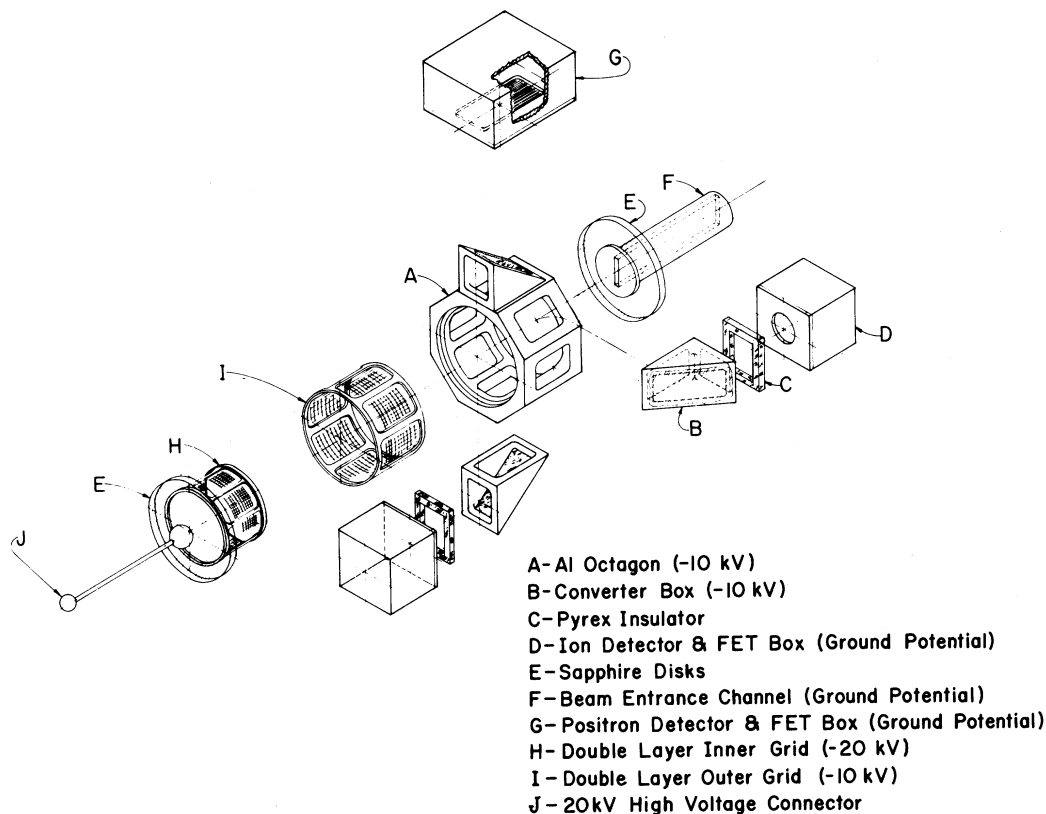
FIG. 5. Exploded view of cell detector assembly. Sapphire disks are held onto the octagon by small brass spring clips. Other items are secured with screws. All joining surfaces are lapped to flatness. Dow Corning silicon-based vacuum grease is used to ensure a vacuum seal of all joints. A copper lip, threaded into the end of the copper beam entrance channel, secures the sapphire disk. The only opening in the bulb is the 0.07×0.95-cm entrance slit. When all joints are properly sealed, the sitting time of the ^{19}Ne in the bulb is 4 sec.

from a double layer of the same stainless steel mesh, makes a slip fit in the inner hole of the Al octagon. The radial distance between inner and outer grids is 0.4 cm. The outer grid, along with the Al octagon and converter boxes, is maintained at -10 keV, thus providing a 25-kV/cm potential gradient for the acceleration of F$^-$ ions. The double-layer grid construction reduces undesirable fringing of electric fields into the interior of the inner grid and converter box. The strong E field at the surface of the inner grid might cause field emission of electrons from any microscopic metal whiskers present on the surface of the grid wires, and thus produce an undesirable background. To reduce this, both grids were gold-plated, and carefully washed in nitric acid, distilled water, and ethanol just prior to installation.

The entire detector cell unit is held by an Al bracket mounted on a brass pedestal inside the 50-liter vacuum chamber, and cooled to 100 °K by thermal contact with an LN$_2$ (liquid nitrogen) res-

ervoir to reduce noise from the e^+ and ion detectors. Thermal contact to the ion detectors is maintained by the copper entrance channel and sapphire end plates (the latter being good thermal conductors but electrical insulators at LN$_2$ temperature).

C. Positron detectors

Large-volume Si(Li) positron detectors are required to provide adequate solid angle and sensitive range for e^+ up to the end-point energy of 2.22 MeV (range 0.42 cm). The dimensions of the sensitive depletion volume, $1.2 \text{ cm} \times 3.0 \text{ cm}$ area by 0.4 cm thickness, were limited by available fabrication techniques at LBL. The detectors operate with a 400 V bias and have an energy resolution of 9 keV.

A typical coincidence e^+ energy spectrum is shown in Fig. 6. A ^{137}Cs source providing internal conversion electrons from ^{137}Ba at 625 keV and 655 keV is used for energy calibration. Discriminators are set to accept all positrons above 0.5 MeV.

D. Recoil ion detection

Detection of $^{19}F^-$-recoil ions requires a highly stable, efficient low-noise system which, in contrast to the positron detectors, must be an integral part of the sealed cell. The ion counters, based on an earlier design[11,12] consist of a converter box with a thin secondary-emission Al foil, a Si(Li) detector plus field-effect transistor preamplifier (FET), and a hollow glass electrical insulator separating the converter and detector boxes. The silicon detectors are 1.27 cm in diameter and 1 mm thick, and have sufficient range to stop 600-keV electrons. The sensitive depletion region is 0.96 mm thick. Cooling of the FET and detector and use of linear gates before mixing signals from all ion detectors resulted in a resolution of 4 keV. A 50 Å gold layer on the detector face, chosen thin enough to allow transmission of 10 keV electrons, is maintained at a 125-V bias.

A typical coincidence event from a decay within the field-free region of the inner grid is shown in Fig. 4. The positron is detected immediately. The ion, having an average recoil energy of 100 eV, drifts slowly in its original recoil direction toward the transparent surface of the inner grid, with drift times ranging from 0 to 1.4 μ sec. Once the ion has passed through the inner grid it is accelerated radially toward the thin window of the converter box, which can collect ions only from the corresponding portion of the inner grid surface. After passing through the outer grid, the 10-keV ion collides at an angle of about 45° with the thin Al window and ejects secondary electrons. The Si(Li) detector is sealed inside the call and is connected with small feedthroughs to the FET in an adjoining box. With the front face of the Si(Li) detector at 125 volts and insulated from the −10
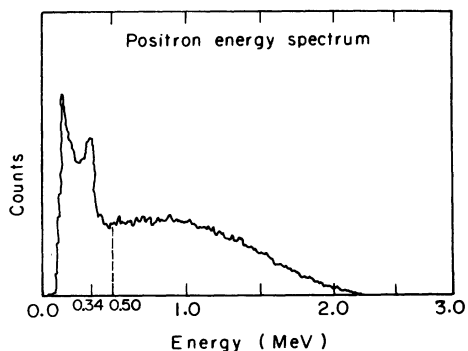
keV converter box, the secondaries are accelerated and to some extent focused toward the Si(Li) detector. An ion is thus detected as a pulse of one or more 10-keV electrons. For decays between the inner and outer grids the ions are immediately accelerated in the radial direction and detected. However these "prompt" ions are delayed less with respect to the corresponding e^+, than ions from inside the inner grid. Thus prompt coincidence events can be distinguished from those originating inside the inner grid.

The number spectrum of secondary electrons ejected by $^{19}F^-$ ions follows a statistical distribution with the average number emitted per stopped ion defined as the secondary emission coefficient γ; with 10-keV F^- ions on Al at 45°, $\gamma \simeq 3$. For one, two, three, etc., electrons ejected, the silicon detector resolves individual lines at 10, 20, 30 keV, etc., as seen in a typical ion coincidence energy spectrum (Fig. 7). The ion discriminator was set at 15 keV to minimize the number of background events due to field emission and prompt low-energy recoil ions. Thus the two-electron peak is the first one seen in Fig. 8.

III. DATA COLLECTION

A. Polarization monitoring and singles data

During the "D" experiment (spin along the beam axis) continuous monitoring of ^{19}Ne polarization is achieved by using the Si(Li) ion detectors to measure the angular correlation term $AP(\langle \vec{J} \rangle /J) \cdot \vec{v}$, where P is the actual polarization. A polarized ^{19}Ne atom decaying inside the cell in an appropriate region can emit a positron which passes

FIG. 6. Observed positron energy spectrum for e^+ in coincidence with $^{19}F^-$. The peak at 340 keV is due to electrons in the detector which have suffered a single Compton-scattering with incoming annihilation photons, (0.511 MeV). The dashed vertical line corresponds to the discriminator setting.
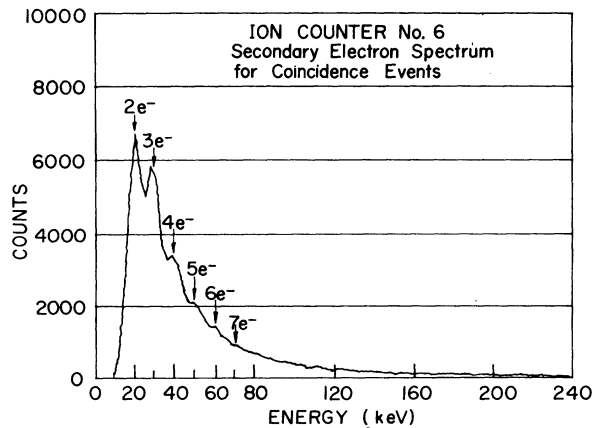
FIG. 7. Secondary electron spectrum generated by collision of $^{19}F^-$ ions with detector foil in e^+-F^- coincidence events. For B and D data, the ion energy discriminator was set at 15 keV to eliminate the large number of single secondary electrons produced by prompt recoil ions.
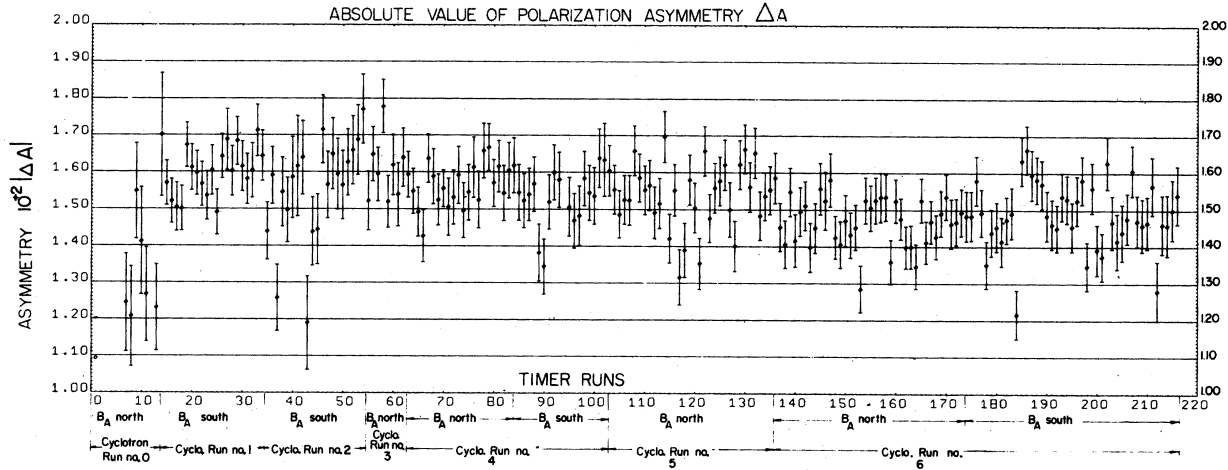
FIG. 8. Absolute value of polarization asymmetry ΔA, plotted versus timer run. ΔA values for cyclotron run No. 0 were lower than in other runs because of poor uniformity and low magnitude of alignment field B_A. These conditions were improved for subsequent runs, and run No. 0 data were not used for determining B and D. D data were not used for any timer run whose values of $|\Delta A|$ deviated by more than 2σ from the experimental average of $(1.52 \pm 0.01) \times 10^{-2}$.

through one of the 1-mm Si(Li) ion detectors, producing a high-energy pulse. The energy lost by an e^+ of 1–2 MeV in this detector is $\simeq 350$ keV, substantially higher than the energy from secondary electrons. With converter boxes and Si(Li) ion detectors facing alternately along the $\pm z$ axis, the difference over the sum in the high-energy singles count rates N_{Si}, from alternate detectors, is proportional to the polarization. Specifically, the latter is given by

$$P = [A S_A G_A \langle v \rangle]^{-1} \Delta_A , \qquad (8)$$

where $A = -0.039 \pm 0.002$ is the previously measured asymmetry coefficient,[3] $S_A = 0.85$ and $G_A = 0.62$ are the calculated backscattering correction and geometry factor for this geometry, respectively, and $\langle v \rangle = 0.96$. Data are taken in both polarization directions ($x_c < 0$ and $x_c > 0$) and we define Δ_A by

$$\Delta_A = \tfrac{1}{2}\left[\left(\frac{N_1 - N_2}{N_1 + N_2}\right)_{x_c > 0} - \left(\frac{N_1 - N_2}{N_1 + N_2}\right)_{x_c < 0} \right] , \qquad (9)$$

where N_1 (N_2) is the sum of the e^+ singles counts for all upstream (downstream) Si detectors for a given time. The singles data consisted of eight channels of e^+ counts, eight channels of ion counts, and eight channels of the 350-keV e^+ counts in the ion detectors. These data were accumulated with a 24-channel scaler system which was automatically read out into the PDP-5 computer every 15 minutes. A plot of Δ_A versus time throughout the experiment gives a measure of consistency for the polarization within the cell (see Fig. 8).

B. Coincidence measurements

Delayed coincidences are recorded for each positron counter E and the four ion counters I oriented at $\pm 90°$ and $\pm 135°$ with respect to E [see Fig. 9 and Tables I(a) and I(b)]. For example, in the "D" experiment the ^{19}Ne nuclear spin is oriented along the $\pm z$ directions. Thus for a given spin direction a finite D would lead to different coincidence counting rates for E_1, I_4, and E_1, I_6. In Table I, (E_1, I_4) is called the first "regular" pair (135°) and (E_1, I_6) is its corresponding "image" for the D experiment. Similarly (E_1, I_3) is the ninth "regular" pair (90°) and (E_1, I_7) is its corresponding "image" pair. In the "B" experiment the ^{19}Ne spin is oriented along the x axis and a different combination of "regular" and "image" pairs is required [see Table I(b)].

Together with each coincidence event, the following information is recorded: The label iden-

(Z axis out of paper)
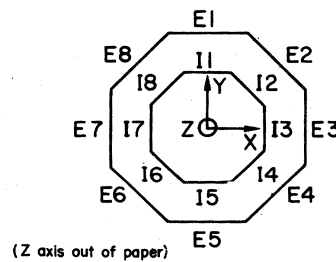
FIG. 9. Schematic view of detector octagonal counter geometry. Positron and ion counter designations E_i and I_j provide a key to the counter pair numbering in Table I.

tifying the coincidence pair, the time delay t between positron and ion, and their respective energies E_e and E_I (see Fig. 10).

Coincidence rates together with the uncorrelated positron and ion singles rates, are accumulated for 15-min intervals in each of the nuclear polarization states (collimator positions $x_c > 0$ and $x_c < 0$). A three-minute measurement of the background, made by moving the collimator far to one side and thus blocking the ^{19}Ne beam, completes each measurement sequence.

Coincidences are accepted with ion delay times between 0 μsec and 4 μsec, as taken on a 5-μsec scale of a time-to-amplitude converter (TAC) with ion signals delayed by 1 μsec to shift the zero. Three types of coincidence events are distinguished: prompts, trues, and accidentals (see Fig. 11). As previously noted, prompts result from decays between the 10-kV and 20-kV grids. No correlation between e^+ and ion directions is possible, and these events (sharply peaked between 1.0 and 1.5 μsec) provide no useful D or B information. True coincidence events result from decays inside the inner (20 kV) grid. Here, correlation information is preserved and delay times in the acceptable range are from 1.6 to 2.6 μsec, depending on the drift path. Prompts and trues can be distinguished, since their overlap in time is small. Accidental coincidences are uniformly distributed in time, and their contribution can be measured by holding the coincidence gate open for times before and after the time interval when trues are expected (0–1 μsec, 3–5 μsec).

Typical coincidence counting rates per 135° pair were 0.7 count/sec and 0.2 count/sec for trues and accidentals, respectively. Typical singles rates per counter were $N_{e^+} = 130$ counts/sec, and $N_I = 2000$ counts/sec, corresponding to a disintegration rate of about 10^4/sec in the cell.

IV. DATA ANALYSIS AND RESULTS

A. D experiment

We consider the positron-ion coincidence pairs l as given in Table I(a) for D. Let the measured coincidence counts corrected for background for the regular and image pairs be y_l and y_l', respectively. We form the quantities

$$\Delta_D^{135} = \frac{1}{16} \sum_{l=1}^{8} \left[\left(\frac{y_l - y_l'}{y_l + y_l'} \right)_{x_c > 0} - \left(\frac{y_l - y_l'}{y_l + y_l'} \right)_{x_c < 0} \right] \quad (10)$$

and

$$\Delta_D^{90} = \frac{1}{16} \sum_{l=9}^{16} \left[\left(\frac{y_l - y_l'}{y_l + y_l'} \right)_{x_c > 0} - \left(\frac{y_l - y_l'}{y_l + y_l'} \right)_{x_c < 0} \right] \quad (11)$$

TABLE I. Positron-ion coincidence pairs.

Pair index	Regular pair Counters $e^+ : F^-$	Image pair Counters $e^+ : F^-$	Geometry factor
(a) Regular and image coincidence pairs for "D" experiment with pair index l			
135° pairs			
1	1 : 4	1 : 6	$G_D^{135} = 0.42 \pm 0.03$
2	5 : 8	5 : 2	
3	7 : 2	7 : 4	
4	3 : 6	3 : 8	
5	2 : 5	8 : 5	
6	6 : 1	4 : 1	
7	8 : 3	6 : 3	
8	4 : 7	2 : 7	
90° pairs			
9	1 : 3	1 : 7	$G_D^{90} = 0.67 \pm 0.03$
10	5 : 7	5 : 3	
11	3 : 5	3 : 1	
12	7 : 1	7 : 5	
13	8 : 2	2 : 8	
14	4 : 6	6 : 4	
15	2 : 4	4 : 2	
16	6 : 8	8 : 6	
(b) Regular and image coincidence pairs for "B" experiment with pair index n			
135° pairs			
1	1 : 4	1 : 6	$G_B^1 = 0.48 \pm 0.03$
2	5 : 2	5 : 8	
3	4 : 1	6 : 1	
4	2 : 5	8 : 5	
90° pairs			
5	1 : 3	1 : 7	$G_B^2 = 0.77 \pm 0.04$
6	5 : 3	5 : 7	
7	3 : 1	7 : 1	
8	3 : 5	7 : 5	

by combining the coincidence observations into experimental asymmetries Δ. In this manner, we introduce a high degree of symmetry into the analysis which eliminates the possibility of systematic errors due to unequal counter efficiencies or possible slight spin misalignment (false B effect).[43]

We then compute D from the formula

$$D = \frac{\dfrac{1}{PS} \left(\dfrac{g_{90}}{G_D^{90}} \Delta_D^{90} + \dfrac{g_{135}}{G_D^{135}} \Delta_D^{135} \right)}{g_{90} + g_{135}} \quad (12)$$

where the g's are statistical weights. Here P is the polarization, S is a backscattering correction, and the G's are geometry factors for the 90° and 135° coincidence pairs. These geometry factors account for the finite spatial volume of the detectors, the finite decay volume, and the momentum distribution of the decay products. A Monte Carlo calculation yields $G_D^{90} = 0.67 \pm 0.03$ and $G_D^{135} = 0.42 \pm 0.02$ for the inner grid used on five cyclotron runs, while $G_D^{90} = 0.77 \pm 0.04$ and $G_D^{135} = 0.56 \pm 0.03$ for an inner grid of smaller diameter used on one cyclotron run.

Total running time for the D measurement was 125 hours, during which 4×10^6 D events were collected in 215 separate polarization cycles. For all of the final D data $P = 0.75 \pm 0.05$ from A mea-
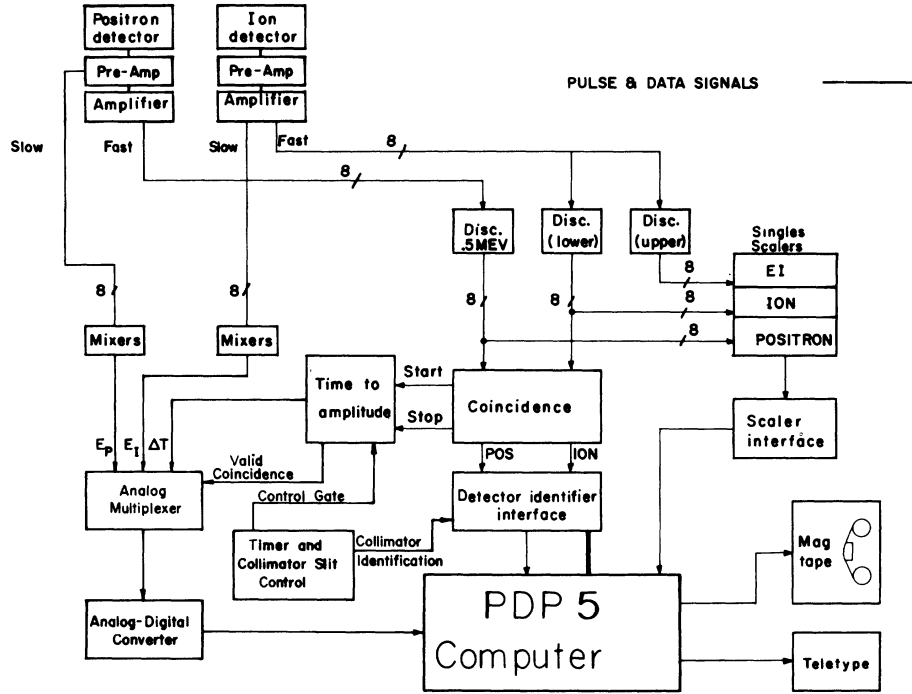
FIG. 10. Schematic diagram of electronics and data-transfer system. For each e^+ above 0.5 MeV threshold in E_i, a fast logic pulse registers the singles count, sets the identification (ID) register labeling the count as coming from E_i, gates off acceptance of all additional e^+ coincidence starts, and starts the time-to-amplitude converter (TAC) for determination of the time delay for possible coincidence. The signal level (energy E_e) from the positron preamp is routed to and held in the multiplexer until the ion completes a coincidence. If no coincidence occurs within 5 μsec, multiplexer and ID register are cleared and e^+ gate opens. An ion pulse I_j causes fast and slow linear amplifier output. Above the ion threshold (2 secondary electrons = 20 keV) the fast output registers the ion singles count, sets the jth ion ID register, gates off acceptance of all additional ion coincidence stops, and stops the TAC, thus registering a coincidence. The fast ion pulse also gates a slow ion signal (energy E_I) from the linear amplifier into the multiplexer. For coincidence, the TAC provides the multiplexer with a time delay Δt. On-line computer analysis of incoming coincidence data is the major source of dead-time in the system. The dead-time approached 50% at the highest counting rates.

surements quoted earlier, and $S = 0.80 \pm 0.14$ as determined from B measurements (see below). The final D data were separated into three e^+ energy intervals: $\delta E_1 = 0.5-1.0$ MeV, $\delta E_2 = 1.0-1.5$ MeV, $\delta E_3 = 1.5-2.21$ MeV. Here 0.5 MeV and 2.21 MeV are the threshold and endpoint energies, respectively. We find

$$D(\delta E_1) = -0.009 \pm 0.006,$$

$$D(\delta E_2) = +0.008 \pm 0.005,$$

$$D(\delta E_3) = +0.010 \pm 0.011.$$

No energy-dependent trend or significant difference exists between these values of D. (See Fig. 1, which also shows the predicted energy dependence of D for an assumed value of the induced tensor term d). Either by combining these values of D or by taking the weighted averages of D's as computed from Δ_D^{90} and Δ_D^{135} for all energies between threshold and endpoint, we obtain

$$D = 0.002 \pm 0.004. \tag{13}$$

The quoted uncertainty in D is purely statistical.

B. B experiment

Referring to Table I(b), let the observed counts for the nth regular and image pairs be ξ_n and ξ_n', respectively. We define

$$\Delta_B(1,2) = \frac{1}{4} \sum_{n=1}^{2} \left[\left(\frac{\xi_n - \xi_n'}{\xi_n + \xi_n'} \right)_{x_c > 0} - \left(\frac{\xi_n - \xi_n'}{\xi_n + \xi_n'} \right)_{x_c < 0} \right], \tag{14}$$

with similar expressions for $\Delta_B(3,4)$, $\Delta_B(5,6)$, and $\Delta_B(7,8)$. Since in the B experiment, the ^{19}Ne spin lies along the x axis, the D correlation averages to zero and the coincidence rate ξ for a given pair depends on B, but also for $n = 3$, 4, 7, 8 it depends on A. The magnitude of A is known from previous experiments; thus B can be determined from the expressions

1.6 μsec

2.6 μsec

COUNTS

0   1   2   3   4   5

TIME (μsec)

A — B — C — A

A - Accidental Background

B - Prompt + Background

C - True + Background
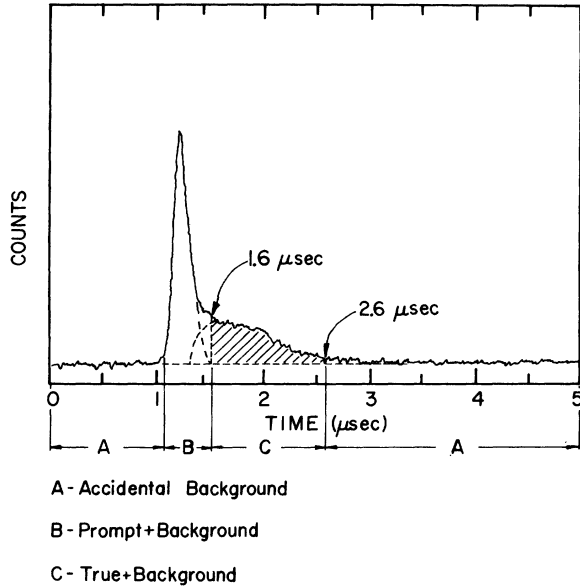
FIG. 11. Time distribution of coincidence events for typical 135° pair, with large inner grid, used for most of the D data. Prompt events are caused by ions orginating between inner and outer grids; these are useless for measuring D and B. Prompt and true events overlap in the region between 1.2 and 1.5 μsec. Only true events in the region between 1.6 and 2.6 μsec were accepted for analysis. Similar time distributions were observed for the small inner grid, and for 90° e^+ -F$^-$ counter pairs.

$$135° \text{ pairs} \begin{cases} BG_B^1 = \dfrac{1}{PS} \Delta_B(1,2), & (15) \\[2mm] (BG_B^2 + AG_{BA}^1) = \dfrac{1}{PS} \Delta_B(3,4); & (16) \end{cases}$$

$$90° \text{ pairs} \begin{cases} BG_B^3 = \dfrac{1}{PS} \Delta_B(5,6), & (17) \\[2mm] (BG_B^4 + AG_{BA}^2) = \dfrac{1}{PS} \Delta_B(7,8). & (18) \end{cases}$$

Actually, since B was already known from previous work, the B measurement serves only as a check on the design and operation of the detector-cell system. A high degree of accuracy is unnecessary, and only $\Delta_B(1,2)$ was actually determined by measurements accumulated over a total of ~10 hours. The value of Δ_B obtained for all positron energies between 0.5 and 2.21 MeV and delay times between 1.6 μsec and 2.6 μsec is

$$\Delta_B = -0.258 \pm 0.015. \tag{19}$$

Using $P = 0.75 \pm 0.05$, $S = 0.85 \pm 0.1$, and $G_B^1 = 0.48 \pm 0.03$, we obtain

$$B = -0.85 \pm 0.17 \tag{20}$$

in agreement with our previous value[3]

$$B = -0.90 \pm 0.13 \tag{21}$$

measured by the decay-in-flight method.

The polarization in the B experiment was determined from direct measurements of the asymmetry parameter A using counters $E2(E8)$ and $E4(E6)$ (see Fig. 9). The uncertainties are attributable to uncertainties in P, G, and particularly to S, rather than to statistics. Note that from Eq.(4) and $|\rho| = 1.60$ with $\phi \approx 180°$, $B_{\text{theo}} = -0.998$.

Alternatively, one may use our present B result as a measure of e^+ (and F$^-$) backscattering in the extremely complex cell geometry. For this purpose we write

$$S = S_e S_I = \frac{(\Delta_B)}{G_B P |B|}, \tag{22}$$

where $|B| = 0.90 \pm 0.13$. The quantities S_e and S_I are scattering correction factors for positions and ions, respectively. The latter quantity is difficult to predict but is determined together with S_e by measuring Δ_B. Inserting $P = 0.75$, $G_B = 0.48$, we find

$$S = 0.80 \pm 0.14,$$

which we assume is valid for the backscattering correction in the D experiment also.

V. CONCLUSIONS

From Eqs. (5) and (13), with $|\rho(^{19}\text{Ne})| = 1.60$, we obtain for the phase angle between axial-vector and vector amplitudes in ^{19}Ne decay

$$\phi_{A,V} = 180.2 \pm 0.4°. \tag{23}$$

This represents a factor of four improvement over our previous result. The quoted error is purely statistical.

Unfortunately the present result is inadequate in precision to test the hypothesis that there exists a T-odd amplitude of relative size 10^{-3} in the weak interaction. To make this test it would be necessary to improve our precision by an order of magnitude, and although we regard this as desirable, it would be totally impractical without major improvements in the present experimental apparatus. Mere increase in the total disintegration rate in the detector cell would not lead to a significant improvement because of rapid increase in the ratio of accidental-to-true coincidences. However, a large increase in the size of the e^+ detectors and a consequent improvement in effective solid angle together with a more efficient data-handling system could possibly lead to a tenfold reduction in the uncertainty in D.

*Work supported by U. S. Atomic Energy Commission.

†Present address: Physics Department, Princeton University, Princeton, New Jersey 08540.

[1] See also D. C. Girvin, thesis, University of California, 1972 [LBL Report No. 731 (unpublished)].

[2] F. P. Calaprice, E. D. Commins, H. M. Gibbs, G. L. Wick, and D. A. Dobson, Phys. Rev. Lett. 18, 918 (1967).

[3] F. P. Calaprice, E. D. Commins, H. M. Gibbs, G. L. Wick, and D. A. Dobson, Phys. Rev. 184, 117 (1969).

[4] B. J. Erozolimski et al., Yad. Fiz. 11, 1049 (1970) [Sov. J. Nucl. Phys. 11, 583 (1970)].

[5] J. D. Jackson, S. B. Treiman, and H. W. Wyld, Jr., Phys. Rev. 106, 517 (1957).

[6] B. R. Holstein, Phys. Rev. C 5, 1529 (1972).

[7] E. D. Commins, Weak Interactions (McGraw-Hill, New York, 1973), p. 96.

[8] C. W. Kim and H. Primakoff, Phys. Rev. 180, 1502 (1969); also L. Maiani, Phys. Lett. 26B, 538 (1968) and N. Cabibbo, Phys. Lett. 12, 137 (1964).

[9] L. Wolfenstein, in Theory and Phenomenology of Particle Physics, edited by A. Zichichi (Academic, New York, 1969), p. 218.

[10] V. Fitch, Princeton University Report No. PURC-4159-53, 1972 (unpublished).

[11] H. M. Gibbs and E. D. Commins, Rev. Sci. Instrum. 37, 1385 (1966).

[12] F. Calaprice and P. Goldsmith (to be published).

Negative-pion photoproduction from neutrons by linearly polarized photons in the first resonance region

K. Kondo, T. Miyachi, K. Ukai, A. Yamamoto,* K. Gotow,† and H. Yoshida‡

Institute for Nuclear Study, University of Tokyo, Tanashi-shi, Tokyo, Japan

S. Kurokawa, H. Muramatsu,§ N. Sasao, and S. Suzuki

Department of Physics, University of Tokyo, Tokyo

M. Kobayashi

National Laboratory for High Energy Physics, Oho-machi, Tsukiba, Ibaraki, Japan

S. Iwata ‖

Department of Physics, Nagoya University, Nagoya, Japan

(Received 23 May 1973)

The angular dependence of the asymmetry for negative-pion photoproduction on neutrons by linearly polarized photons has been measured for photon energies 260, 300, 350, 400, 450, and 500 MeV at center-of-mass angles 60°, 75°, 90°, 150°, and 120°. The results are compared with theoretical models of low-energy single-pion photoproduction. The observed asymmetry below 400 MeV shows good agreement with predictions of dispersion-theoretical models by Berends, Donnachie, and Weaver and by Schwela. The asymmetry values in the 400–500 MeV energy region suggest that smaller M_{1-} amplitude is more favorable.

I. INTRODUCTION

In a systematic study on single-pion photoproduction from nucleons, one needs information about the pion production on neutrons $\gamma n \to \pi^- p$, $\pi^0 n$ which is still lacking to allow quantitative amplitude analyses. There has been renewed interest in the neutron-target processes, since Sanda and Shaw[1] suggested that the possible existence of isotensor electromagnetic current of the hadrons could explain an anomalous dip found in the difference between the total cross sections for the two processes, $\gamma n \to \pi^- p$ and $\gamma p \to \pi^+ n$, in the first-resonance region. An argument by Berardo et al.[2] that the detailed balance in the $\gamma n \to \pi^- p$ process seems to be violated has stimulated further investigation on the $\gamma n \to \pi^- p$ process.